



Range Versus Surface Denoising of Terrestrial Laser Scanning Data for Rock Discontinuity Roughness Estimation

Maja Bitenc¹ · D. Scott Kieffer¹ · Kourosh Khoshelham²

Received: 13 June 2018 / Accepted: 7 February 2019 / Published online: 27 February 2019
 © The Author(s) 2019

Abstract

Surface roughness represents a major component of rock discontinuity shear strength. To achieve comprehensive, accurate, and efficient estimates of in situ discontinuity roughness, the traditional contact measuring methods are being replaced by advanced remote-sensing technologies. Terrestrial laser scanner (TLS) is well suited for measuring large inaccessible discontinuities; however, inherent TLS range noise strongly influences the surface details and roughness estimation. The aim of this research is to establish an optimal wavelet-denoising procedure for the TLS data acquired with different scanning configurations (range and incidence angle), and for rock discontinuities having different roughness characteristics and surface reflectivity. The conventional discrete wavelet transform and stationary wavelet transform in combination with four threshold selection methods are applied on TLS data in the direction of range measurements (range denoising) and in the direction perpendicular to the best-fit plane (surface denoising). The performance of the denoising procedures is assessed by comparing the range and surface-denoised TLS surfaces with reference surfaces acquired with the Advanced TOpometric Sensor. Comparative analyses of the roughness calculated according to the angular thresholding method (Grasselli, in Shear strength of rock joints based on quantified surface description, Ph.D. thesis, EPF Lausanne, Lausanne; Grasselli, Shear strength of rock joints based on quantified surface description, Ph.D. thesis, EPF Lausanne, Lausanne, 2001) indicate that all the denoising methods improve the roughness estimated from the TLS data appreciably; however, the level of improvement depends intrinsically on geometrical characteristics of the rock surface and scanning configuration. Range denoising has been found to provide more reliable noise estimations.

Keywords Rock discontinuity roughness · Angular thresholding method · Terrestrial laser scanning · Image denoising

List of Symbols

θ^*	Apparent asperity angle
θ_{\max}^*	Maximum apparent asperity angle
A_{θ^*}	Total potential contact area ratio
A_0	Surface area defined by an apparent dip greater than 0° normalized with respect to the total area of the surface

C	Dimensionless empirical fitting parameter calculated via a non-linear least-squares regression
G	Grasselli parameter
σ	Noise level
σ_e	Noise-level estimation
T	Threshold value
T_0	Threshold chosen according to one of the threshold selection methods for a signal model including white noise ($\sigma = 1$)
cD_1	First-level detail coefficients
β	Analysis direction for which the Grasselli parameter is computed
G_{ATOS}	Grasselli parameter of reference ATOS surface
G_{TLS}	Grasselli parameter of TLS surface

✉ Maja Bitenc
 bitenc@tugraz.at
 D. Scott Kieffer
 kieffer@tugraz.at
 Kourosh Khoshelham
 k.khoshelham@unimelb.edu.au

¹ Institute of Applied Geosciences, Graz University of Technology, Rechbauerstrasse 12, 8010 Graz, Austria

² Department of Infrastructure Engineering, University of Melbourne, Engineering Block B, Parkville, Melbourne 3010, VIC, Australia

1 Introduction

Surface roughness represents a significant component of discontinuity shear resistance and influences the overall deformation behaviour of jointed rock masses. Since surface roughness is scale- and direction-dependent (ISRM 1978), it is preferable to perform measurements in the anticipated shear direction and at the engineering scale of interest. Larger scale roughness features are referred to as “waviness” and represent surface irregularities with a wavelength greater than about 10 cm (Priest 1993). Smaller scale features are referred to as “unevenness” and cover finer features, which are superimposed on the waviness.

In the laboratory, roughness is traditionally measured on small rock samples (up to 50 cm length) using several measuring methods such as a mechanical profilometer (ISRM 1978), shadow profilometer (Maerz et al. 1990), laser profilometer (e.g., Huang et al. 1992), or a structured light projection method using a stereo-topometric camera, such as the Advanced TOPometric Sensor—ATOS (e.g., Grasselli et al. 2002). In situ discontinuity roughness is routinely estimated visually (using a catalogue of joint profiles), or measured using the traditional contact-based methods, e.g., compass and disc-clinometer method (Fecker and Rengers 1971), and linear mechanical profiling using a straight edge or contour gauge (Barton and Choubey 1977; Milne et al. 2009). The traditional in situ measurements provide analogue, discrete data that are restricted to an accessible area. In contrast, remote-sensing technologies such as photogrammetry and terrestrial laser scanning (TLS) allow the in situ acquisition of a large and remote surface in a short period of time (e.g., Poropat 2009). These methods are able to characterize the 3D surface structure, which is represented as a dense and precise point cloud that can be used for surface roughness estimation at different scales and along any direction.

The traditional stereo-photogrammetry has been used for roughness measurements for nearly 30 years (Lee and Ahn 2004; Haneberg 2007; Baker et al. 2008). New developments in computer vision methods, in particular Structure from Motion (SfM) combined with dense image matching (Hartley and Zisserman 2003; Carrivick et al. 2016), allow 3D reconstruction of a detailed surface from an array of unconstrained images. For SfM and dense image matching, the surface is preferably photographed at close range and from many different positions and orientations, which is not always possible in constrained terrain. Furthermore, reference points (visible on the acquired photos) need to be established and measured to define the linear scale, and setting the points can be time-consuming and precarious in rugged alpine terrain.

Terrestrial laser scanner has been successfully applied to in situ roughness measurements (Fardin et al. 2004;

Renard et al. 2006; Rahman et al. 2006; Tesfamariam 2007; Haneberg 2007; Candela et al. 2009; Khoshelham et al. 2011; Pollyea and Fairley 2011; Mills and Fotopoulos 2013). While reasonable results have been obtained in quantifying waviness (Fardin et al. 2004), finer details of unevenness have been hindered by data precision and laser footprint size. The data precision mainly depends on the inherent random range error (noise), which results in an overestimation of surface roughness (e.g., Kulatilake et al. 2006; Poropat 2009; Khoshelham et al. 2011). The challenge is to eliminate noise, but preserves surface details.

With TLS, noise has typically been removed by surface interpolation techniques such as averaging the TLS range measurements (Schulz et al. 2008), orthogonal least squares (Fardin et al. 2004; Pollyea and Fairley 2011), the robust interpolation method RANSAC (Grasselli et al. 2002), or Fast Radial Basis Function (Rahman et al. 2006; Tesfamariam 2007). The disadvantage of interpolation methods is that irregular rock surfaces are smoothed and some topographic details are lost. By reducing the spatial complexity of a 3D randomly scattered point cloud (i.e., gridding to a regular 2.5D mesh), a wider range of image processing algorithms can be applied. An overview of image denoising methods and further references can be found in (Buades et al. 2005; Smigiel et al. 2011; Zhang et al. 2014).

Wavelet-denoising methods, including the discrete wavelet transform (DWT) and the wavelet packet (WP), have been applied to profile measurements subjected to fractal-based roughness length analysis and have been found to provide better roughness estimates than if no denoising was performed (Khoshelham et al. 2011). An important advantage of DWT compared to the other denoising techniques is that the TLS noise level is correctly estimated from the raw data (Bitenc et al. 2015a). Prior research has focused on wavelet denoising in a direction perpendicular to the best-fit plane (hereafter referred to as surface denoising). However, denoising in the range direction (hereafter referred to as range denoising) is considered preferable, since noise mainly relates to range.

Despite prior research showing the applicability of TLS to quantifying roughness, thorough investigations concerning the influence of noise and the choice of optimal denoising procedure under conditions of variable range, scanning direction (incidence angle), surface roughness, and reflectivity have been lacking. This contribution evaluates TLS data acquired for four rock samples having different roughness and reflectivity characteristics, and at different scanning ranges and directions. Reference data were measured with ATOS and the roughness was calculated according to the angular threshold method (Grasselli 2001). The objectives of this research are to:

- investigate the influence of intrinsic TLS data noise on roughness (noise effect);
- evaluate TLS noise estimations derived from the data itself using DWT and stationary wavelet transform (SWT), in the range and surface roughness measuring directions;
- analyse the performance of eight denoising methods including DWT and SWT, in combination with four threshold selection methods that are applied in range and surface roughness measuring directions.

The success of wavelet-denoising procedures is evaluated through a comparative analysis of reference ATOS and denoised TLS surfaces and their derived roughness values. The goal is to identify optimal TLS denoising procedures for different rock surfaces and scanning configurations.

2 Parameterizing Rock Discontinuity Roughness

Discontinuity surface roughness describes the local departures of the actual surface from planarity or any higher order reference surface. Roughness can have a prevailing influence on the shear strength, particularly in cases of low normal stress combined with unfilled discontinuities. However, the parameterization of roughness, to fully capture the influence of roughness on shear strength, remains a challenge; parameterization needs to consider that roughness is direction and scale dependent.

Since the introduction of rock surface roughness into a shear strength criterion as an asperity angle (Patton 1966), a variety of rock surface roughness parameters have been developed. They are either 1D (profiles) or 2D (surfaces), and are based on empirical data (e.g., Patton 1966; Barton and Choubey 1977; Bandis et al. 1983; Grasselli 2001), statistical data (e.g. Myers 1962; Wu and Ali 1978; Krahn and Morgenstern 1979; Tse and Cruden 1979; Reeves 1985; Belem et al. 2000; Renard et al. 2006), or fractal analysis (e.g., Lee et al. 1990; Power and Tullis 1991; Huang et al. 1992; Seidel and Haberfield 1995; Kulatilake et al. 2006; Baker et al. 2008). Some parameters describe only the roughness amplitude, while others also include direction and/or scale dependence.

The empirical roughness parameter developed by Grasselli (2001), hereafter referred to as the Grasselli parameter (G), has been adopted in this research, since it quantifies the direction dependence of roughness, is applicable to rock surfaces, and is least sensitive to data noise (Bitenc et al. 2015c). The Grasselli parameter is based on an angular threshold concept and was initially developed to identify potential contact areas during direct shear testing of artificial tensile rock fractures. Studying

the damaged areas after shear testing, it was found that only the parts of the surface that face the shear direction and are steeper than a threshold inclination provide shear resistance. Surface data are first transformed into the average discontinuity plane (or shear plane) coordinate system and modelled with Delaunay triangulation. For each triangle, an apparent dip θ^* is calculated according to the specific analysis direction and the shear plane. The sum of triangulated areas that are steeper than a certain value of θ^* (denoted as A_{θ^*} and referred to as the total potential contact area ratio) is plotted against θ^* (Fig. 1).

Based on curve fitting and regression analysis of A_{θ^*} as a function of θ^* , G is calculated as follows:

$$G = \frac{\theta_{\max}^*}{C + 1}, \quad (1)$$

where θ_{\max}^* is the maximum apparent asperity angle of the surface in the shear (analysis) direction and C is the dimensionless empirical fitting parameter calculated via non-linear least-squares regression. To account for surface anisotropy, the following correction has been proposed (Tatone and Grasselli 2009):

$$G = 2A_0 \frac{\theta_{\max}^*}{C + 1}, \quad (2)$$

where A_0 is the surface area defined by an apparent dip greater than 0° , normalized with respect to the total area of the surface. In the normal case that A_0 equals 0.5, the roughness matrix reduces to the simplified version in Eq. (1). The expression in Eq. (2) is used in this research to estimate the surface roughness.

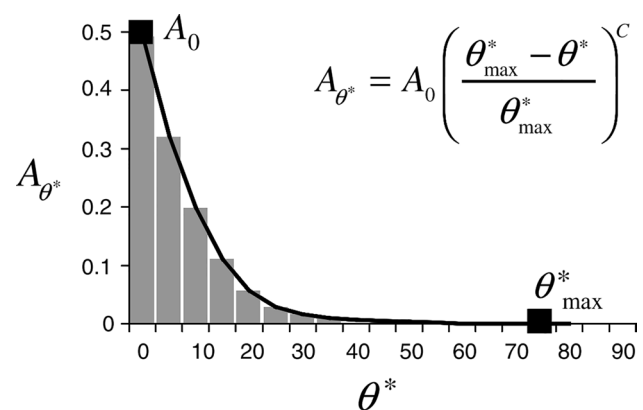


Fig. 1 Cumulative distribution of potential contact area ratio A_{θ^*} as a function of the various threshold values of apparent dip θ^* ($^\circ$) (Grasselli 2001)

3 Denoising Laser Range Data Using Wavelets

Terrestrial laser scanner principles and limitations are enumerated below, along with the wavelet-denoising procedure.

3.1 Terrestrial Laser Scanning

Terrestrial laser scanner has a ranging and scanning unit for performing measurements. Range can be measured based on roundtrip time-of-flight (TOF scanner) or phase shift (phase scanner). Phase scanners are more precise (on the order of 1 mm), but have a limited range of a few tens of metres. TOF scanners have a precision in the order of 3–5 mm and range of up to a few kilometres, and are commonly used for rock mass characterization. The scanning unit consists of a motor-driven head with rotating mirrors to spatially redirect the laser beams to cover large areas. With TLS, the position and intensity of thousands of points can be recorded within a few seconds, at an angular resolution typically smaller than 0.01° . The point position is originally recorded in polar coordinates, which are, in real time, recalculated and stored as Cartesian coordinates. Intensity is a relative unit less number and is influenced mainly by the reflectance of the target surface and the laser scanning configuration (Wagner 2005).

In general, the ability for TLS to capture surface roughness details depends on: the effective spatial resolution of TLS points and the error (noise) associated with the measurements. The effective resolution depends on sampling interval and laser beam footprint size (Lichti and Jamtsho 2006), and causes roughness underestimation (smoothing effect), while the presence of intrinsic TLS noise results in roughness overestimation (noise effect).

TLS point cloud errors arise from the following sources (Soudarissanane et al. 2011): (1) range and scan angle errors; (2) the scanning configuration and the material reflectivity; and (3) environmental conditions including lighting, humidity, and temperature. With systematic errors properly calibrated and removed, the remaining random error represents the measurement noise. Wujanz et al. (2017) showed that the range noise σ can be jointly considered as a function of backscattered signal strength or intensity I and proposed a

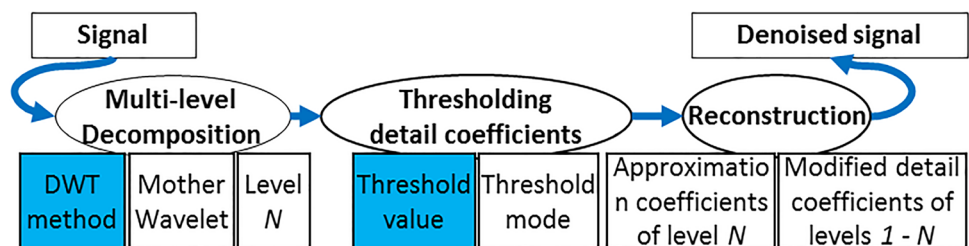
one-term power series model $\sigma = a \times I^b$, where the unknown parameters a and b are determined within least-squares regression.

3.2 Wavelet Denoising

The wavelet transform (WT) is an extension of the classical Fourier transform. The WT basis functions (mother wavelets) exist in space, frequency, and amplitude, are irregular and asymmetric, and have limited duration. This makes the WT particularly suitable for natural rock surfaces that typically contain finite, non-periodic, and/or non-stationary signals that are characterized by discontinuities and sharp peaks. Scaling and shifting are central concepts of the WT. Scaling refers to the process of stretching or shrinking the wavelet in space, thus changing the frequency. Shifting a wavelet refers to delaying or advancing the onset of the wavelet along the length of the signal. The input signal is transformed into the space–frequency domain, where the particular unwanted or unneeded space or frequency components can be removed. The discrete wavelet transform (DWT) was developed to enable unique signal reconstruction using orthogonal wavelets and has, therefore, been widely applied for denoising and compression (Donoho 1995). The DWT has been adopted in this research.

The main steps of wavelet denoising involve multi-level signal decomposition, thresholding of detail coefficients, and signal reconstruction (Fig. 2). The signal is first decomposed (filtered) into several levels ($j = 1, \dots, N$) of approximation coefficients, cA_j , and detail coefficients, cD_j . This is performed using a DWT, a mother wavelet (filter), and N decomposition levels. An example of two-level DWT is shown in Fig. 3. Approximation and detail components contain low- and high-frequency contents, respectively. Next, an appropriate threshold value is calculated and cD_j values below the threshold are discarded, because they are assumed to represent only noise. The cD_j values above the threshold can be reduced, depending on the chosen threshold mode. The thresholding is intended to suppress the noise and preserve the original surface. Finally, the surface is reconstructed using the original cA_N of the last level N and the modified cD_j from levels 1 to N ($j = 1, \dots, N$).

Fig. 2 Main steps of wavelet denoising



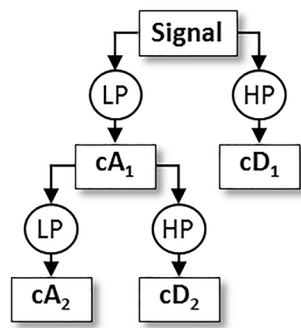


Fig. 3 Two-level ($N=2$) discrete wavelet transform (DWT) decomposition of a signal using high-pass (HP) and low-pass (LP) filters

In this research, two DWT methods are tested; the conventional decimated DWT (e.g. Daubechies 1992; Donoho 1995) and its undecimated version, referred to as the stationary wavelet transform, or SWT (Coifman and Donoho 1995). Advantages of SWT are that it is shift invariant, provides more precise information regarding frequency localization, enables direct correlation of the space scale to the original data, reduces the edge effect (Coifman and Donoho 1995; Buades et al. 2004), and shows superior performance for image denoising (Gyaourova et al. 2002; Starck et al. 2004). For denoising 3D rock surfaces, 2D DWT and 2D SWT are used, where the input signal is a 2.5D grid (an image).

The threshold value (T) is a key to successful wavelet denoising, and is, in general, calculated as follows:

$$T = \sigma \times T_0, \quad (3)$$

where σ is the standard deviation of the noise and T_0 is the threshold chosen according to one of the threshold selection methods. In the work presented herein, the local fixed-form universal (Donoho and Johnstone 1995) and the global penalised (Birgé and Massart 1997) threshold selection methods are tested. The local fixed-form universal threshold is used most commonly if the signal-to-noise ratio is small. The global-penalised threshold is a variant of the fixed-form and includes an adjustable (sparsity) parameter. A higher

sparsity parameter returns a higher threshold, resulting in more coefficients being eliminated and a sparser (smoother) signal representation. In this research, the default sparsity parameter values for penalised low, penalised medium, and penalised high thresholds were tested. The noise level σ is estimated as a robust standard deviation of first-level detail coefficients cD_1 (Donoho and Johnstone 1995) and is defined as σ_e :

$$\sigma_e = \text{median}(|cD_1|)/0.6745. \quad (4)$$

4 Experiments and Results

The experiments described below were conducted to evaluate the effect of TLS noise on rock surface roughness and to analyse TLS noise details. The experiments were also designed to investigate optimal wavelet-denoising procedures in relation to: (1) threshold selection method (fixed form or penalised); (2) wavelet transform (DWT or SWT); and (3) denoising direction (range or surface denoising). Comparative analyses of noisy and denoised TLS data, and ATOS data based on the Grasselli parameter values were performed for different scanning configurations, and rock reflectivity and roughness characteristics.

4.1 Data Acquisition

The four rock samples comprising the experimental data set are shown in Fig. 4, along with the reference direction for calculating the Grasselli parameter.

Each sample was fixed on the wooden board equipped with four 10 cm square TLS black–white targets on top of which a 7 mm circular ATOS black–white target was pasted (see Fig. 5, right). The board with samples and targets was simultaneously scanned with the terrestrial laser scanner Riegl VZ400 and the optical 3D coordinate measuring sensor GOM ATOS I (Fig. 5). The key technical specifications of these sensors are summarized in Table 1. The principles of terrestrial laser scanner and 3D optical scanner are, in more detail, explained in, e.g., (Pfeifer and Briese 2007)

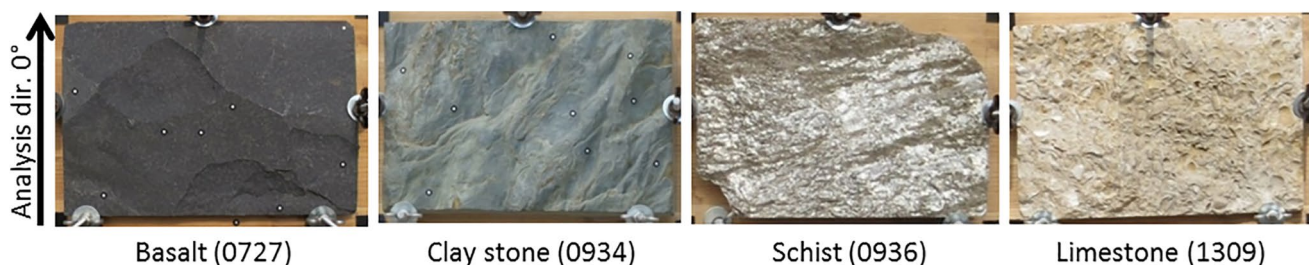


Fig. 4 Rock samples 20×30 cm in plan dimensions mounted to a wooden board. The reference (zero) analysis direction for calculating the Grasselli parameter is indicated in the left

and (Hong et al. 2006), respectively. The black–white targets included on the sample mounting board were needed to co-register the TLS and ATOS data in postprocessing. High-precision TLS target centers were measured in the point cloud by applying an algorithm based on image matching (Kregar et al. 2013) and ATOS target centers were identified automatically with built-in software.

For each sample, the TLS scans were acquired at 10 m intervals in the range of 10–60 m. For each range position, scans were performed perpendicular and obliquely to the mean rock plane (exception of an oblique scan that was not performed at the 60 m range, because of the low point resolution), resulting in 11 data sets. For the oblique orientations, the mean sample plane was rotated about a vertical axis and the angle between the plane normal and the TLS line of sight was between 25° and 47°. Table 2 summarizes the scanning configurations and is consistent with terminology presented in data graphs.

The scanning resolution on the rock surface ranged from approximately 0.2–2 mm. For a filtered 3D point cloud,

Cartesian (X_S, Y_S, Z_S) and polar (Φ, Θ, R) coordinates along with raw intensity values were exported in the scanner coordinate system.

ATOS data were acquired at a range of approximately 0.7 m in an indoor laboratory environment. Changing the position of sensor head with respect to the rock sample, shadow zones were eliminated, and a full and detailed 3D surface model was acquired. 3D images were automatically merged into a single point cloud with the help of the circular black and white targets (diameter 7 mm) stuck on the rock surface (see Fig. 4, basalt and clay stone samples). The ATOS high point density was reduced to the TLS point density of approximately 1 point/mm² using the subsample tool in CloudCompare (2018) to eliminate the influence of data resolution on roughness comparisons.

4.2 Data Processing

The overall workflow involved in wavelet denoising of TLS data and performing a comparative analysis of Grasselli

Fig. 5 The Riegl VZ400 (left), GOM ATOS I (middle) measurement set-ups and the 10 cm squared TLS black–white target with 7 mm circular ATOS black–white target pasted in the centre (right)



Table 1 Specifications of Riegl VZ400 and GOM ATOS I sensors

	Riegl VZ400	GOM ATOS I
Measurement range	1.5–500 m (at 80% reflectivity)	0.65–1 m
Precision/accuracy	3 mm/5 mm	0.007–0.07 mm/unknown
Spot or pixel size	6.5 mm beam aperture +0.3 mrad beam divergence	0.04–1.00 mm
Point spacing	Min. vertical and horizontal angular scanning step is 0.0024°	0.04–1.0 mm
Measurement rate (points/s)	42 k (long-range mode) or 122 k (high-speed mode)	1000 k
Measuring FOV or area	360°×100°	30×40 mm–1000×800 mm

Table 2 Summary of 11 TLS scanning configurations; 6 distances from 10 to 60 m and two scanning directions, perpendicular (Per) and oblique (Obl)

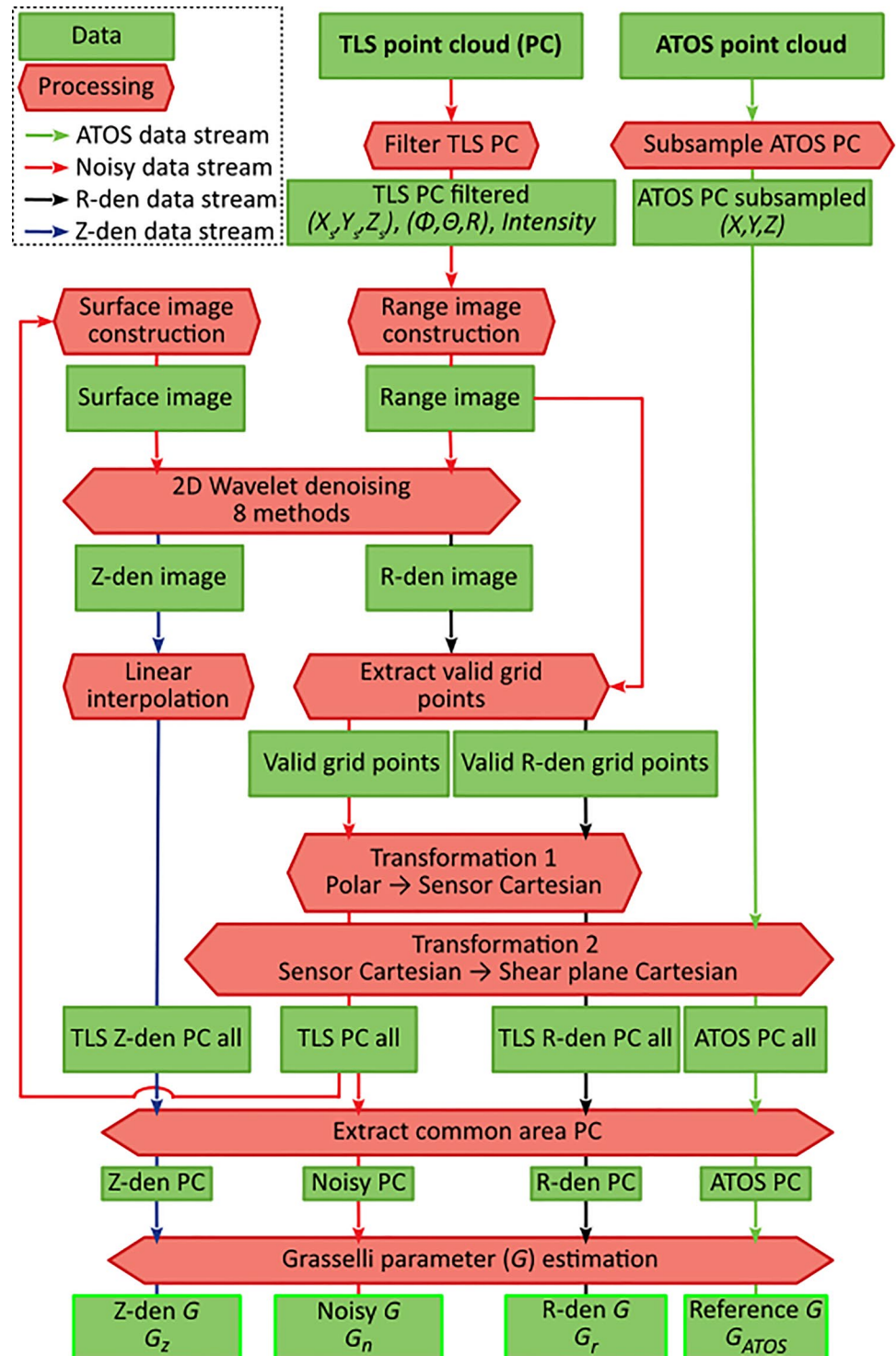
Scanning configuration	1	2	3	4	5	6	7	8	9	10	11
Range (m)	10		20		30		40		50		60
Scan. direction	Per	Obl	Per	Obl	Per	Obl	Per	Obl	Per	Obl	Per

roughness parameters is depicted in Fig. 6 and enumerated below. The processing was performed in Matlab.

Wavelet denoising in 2D is an image processing technique requiring a full matrix (an image). Therefore, a range image was constructed from randomly scattered TLS points (Φ , Θ , R) as follows:

1. In the $\Phi\Theta$ -plane, a rectangle including the rock surface to be denoised plus a surrounding buffer zone was defined. The buffer zone is necessary to prevent edge artefacts from contaminating the results of rock surface denoising.
2. Within the rectangle, a regular grid was created with an angular spacing equal to 1 mm at the corresponding

Fig. 6 Data processing workflow for wavelet denoising of TLS data and performing a comparative analysis of Grasselli roughness parameters



scanning range. The grid point spacing of 1 mm was selected to be equal to or larger than the scanning interval for most of the TLS data sets. Creating a regular grid assured uniform point density among the TLS data sets.

- For each grid point, the range value was interpolated using the Nearest-Neighbour (NN) method.

In 2D wavelet denoising, range image was decomposed with the two wavelet transform variants, DWT and SWT, applying the most general and widely used Daubechies wavelet db3. The number of decomposition levels was determined according to the range image size and was set to 3. The DWT and SWT detail coefficients were then thresholded with the local fixed form and three global-penalised thresholds, penalised high, medium, and low, respectively. All thresholds were applied in the hard mode, following the previous findings that hard thresholding is more suitable for rock surface roughness estimation than soft thresholding (Khoshelham et al. 2011; Bitenc et al. 2015a). This denoising process resulted in a new set of range-denoised (R-den) images.

For surface reconstruction, only the grid points, which have an original TLS point closer than the defined angular spacing, were used. These subsets of grid points are referred to as valid grid points. For surface denoising, and roughness estimation and comparison, polar coordinates of valid grid points were transformed to Cartesian coordinates. These transformed TLS point clouds and the ATOS point cloud were then co-registered in a common coordinate system. It was defined by the targets on the wooden board and it is referred to as the mean plane coordinate system.

A surface image was created analogous to range image construction, except a rectangular area was defined in the mean plane. Following the wavelet-denoising procedure for range image, the surface-denoised (Z-den) images are obtained. To preserve point distribution in the mean plane, the denoised Z-values were linearly interpolated from Z-den images, resulting in the Z-den point cloud.

Noisy, R-den, Z-den, and ATOS point clouds within an identical rectangular area, which was defined in the mean plane coordinate system and is referred to as the common area, were used for roughness comparisons. The Grasselli parameter (G) was calculated for 72 analysis directions (β_i , $i = 1, \dots, 72$) spanning 5° increments. The resulting Grasselli parameters are denoted as G_n for the noisy data set, G_r for R-den and G_z for Z-den data sets, and G_{ATOS} for the ATOS data set. The accuracy of roughness estimates for noisy and denoised TLS surfaces G_{TLS} was judged by comparing G_{TLS} to G_{ATOS} , and calculating a mean relative difference across all the analysis directions. This measure is referred to as the Grasselli parameter estimation error and is expressed as follows:

$$\text{error (\%)} = \frac{1}{72} \sum_{i=1}^{72} \left(\frac{G_{TLS, \beta_i} - G_{ATOS, \beta_i}}{G_{ATOS, \beta_i}} \times 100 \right). \quad (5)$$

4.3 Results and Discussion

Details regarding rock surface representations, TLS noise effects, noise estimation, and optimal denoising procedure for rock discontinuity roughness estimation are summarized below.

4.3.1 Rock Surface Representations

For visual impressions of the rock samples, Fig. 7 shows the triangulated ATOS surfaces (Fig. 7a–d) and representative examples of noisy (Fig. 7e–h) and range-denoised (Fig. 7i–l) TLS surfaces. Noisy surfaces represent TLS data acquired at a range of 30 m in the perpendicular direction, and the *range-denoised* surfaces were obtained using the SWT with penalised high threshold, *R-den SWTph*. The differences of ATOS surface and TLS noisy (dZ_{noisy}) and denoised surfaces ($dZ_{\text{R-den}}$), are shown in Fig. 7, m–p and r–u, respectively. Values of dZ_{noisy} are larger in areas of fast changing morphology, due to the lower resolution of TLS data. High dZ_{noisy} values appear randomly across the area of sample 0936 and are probably due to variations in surface reflectivity. The pattern of $dZ_{\text{R-den}}$ values corresponds to the pattern of dZ_{noisy} . In addition, in case of sample 0727, higher $dZ_{\text{R-den}}$ values can be observed along surface discontinuities (ridges), which indicate that wavelet denoising smoothes sharp edges. Medians and robust standard deviations (robust STD) of height differences for the 11 scanning configurations are presented in Table 3.

Negative median height differences indicate systematic co-registration errors, which result from uncertainties of TLS target centre estimation (Kregar et al. 2013), but do not influence surface roughness values. The robust STD of dZ_{noisy} values is an indicator of TLS noise level, and attenuates after range denoising is performed.

4.3.2 TLS Noise Effect on the Grasselli Parameter

The Grasselli parameter was computed for reference ATOS data (G_{ATOS}) to obtain insight to the sample roughness characteristics, and to facilitate roughness comparisons. Figure 8 depicts the direction-dependent G_{ATOS} for the four rock surfaces, and Table 4 summarizes the common area size, and median robust STD values of G_{ATOS} for all analysis directions. Sample 1309 is the roughest, with the median value almost three times higher than the smoothest sample 0727. Sample 1309 also has the least variability with analysis direction as indicated by the low robust STD. The robust STD for sample 0936 shows the highest roughness anisotropy.

G_{ATOS} values were compared to G_n to study the effect of TLS noise on roughness. As shown in Fig. 9, the Grasselli parameter is systematically overestimated for all four

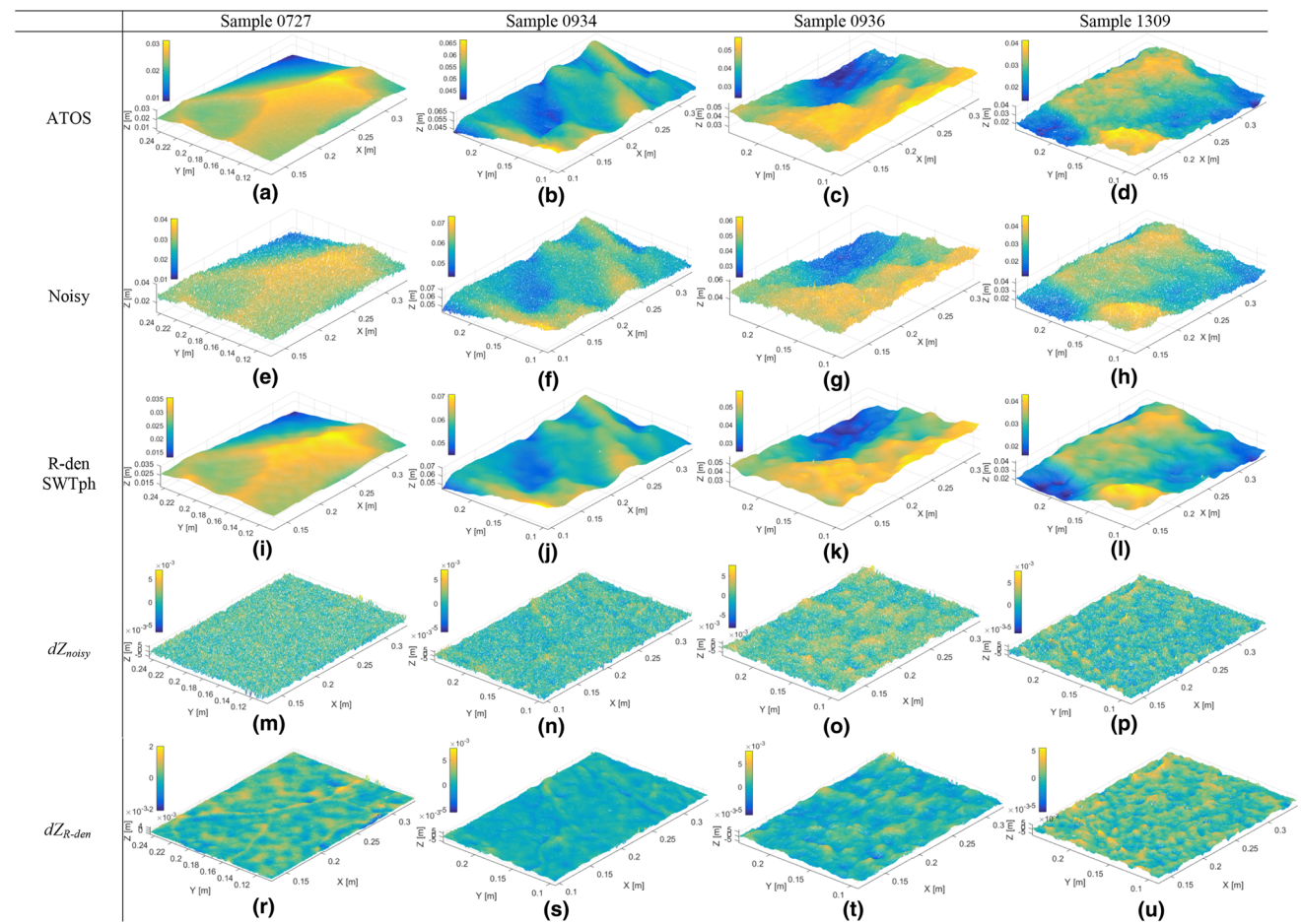


Fig. 7 Rock sample surface representations: **a–d** ATOS surfaces, **e–h** representative TLS noisy surfaces, **i–l** range-denoised TLS surfaces using SWT with penalised high threshold, R-den SWTph, **m–p** sur-

face differences dZ_{noisy} (ATOS—noisy surface), and **r–u** surface differences $dZ_{\text{R-den}}$ (ATOS—R-den SWTph)

Table 3 Height differences (median \pm robust STD in millimetres) of ATOS and TLS noisy surfaces (dZ_{noisy}), and range-denoised surfaces using SWT with penalised high threshold ($dZ_{\text{R-den}}$), for the 11 scanning configurations (Scan. Conf.) and the 4 rock samples

Scan. conf.	Sample 0727		Sample 0934		Sample 0936		Sample 1309	
	dZ_{noisy}	$dZ_{\text{R-den}}$	dZ_{noisy}	$dZ_{\text{R-den}}$	dZ_{noisy}	$dZ_{\text{R-den}}$	dZ_{noisy}	$dZ_{\text{R-den}}$
1	-5.3 ± 1.0	-5.3 ± 0.4	-4.7 ± 1.2	-4.7 ± 0.7	-1.6 ± 1.5	-1.6 ± 1.0	-1.7 ± 1.5	-1.7 ± 1.0
2	-4.3 ± 0.9	-4.4 ± 0.5	-3.9 ± 1.0	-3.9 ± 0.6	-1.6 ± 1.4	-1.6 ± 1.0	-1.2 ± 1.2	-1.2 ± 0.9
3	-5.0 ± 1.0	-5.0 ± 0.4	-4.2 ± 1.5	-4.3 ± 1.3	-1.7 ± 1.5	-1.8 ± 1.2	-2.0 ± 1.4	-2.0 ± 1.1
4	-3.8 ± 0.9	-3.9 ± 0.6	-4.2 ± 1.1	-4.2 ± 0.8	-0.7 ± 1.3	-0.8 ± 1.1	-1.5 ± 1.3	-1.5 ± 1.0
5	-4.8 ± 1.2	-4.9 ± 0.4	-4.5 ± 1.1	-4.5 ± 0.6	-1.4 ± 1.4	-1.5 ± 1.1	-1.6 ± 1.5	-1.6 ± 1.2
6	-3.8 ± 1.1	-3.8 ± 0.6	-3.6 ± 1.2	-3.6 ± 0.8	-1.1 ± 1.4	-1.1 ± 1.2	-1.1 ± 1.4	-1.2 ± 1.2
7	-3.8 ± 1.5	-3.8 ± 0.5	-3.6 ± 1.3	-3.6 ± 0.7	-1.4 ± 1.4	-1.4 ± 1.1	-1.9 ± 1.7	-1.9 ± 1.4
8	-2.3 ± 1.4	-2.4 ± 0.6	-2.0 ± 1.5	-2.0 ± 1.0	-0.4 ± 1.4	-0.4 ± 1.3	-1.6 ± 1.6	-1.6 ± 1.4
9	-2.9 ± 1.8	-3.0 ± 0.5	-2.4 ± 1.7	-2.4 ± 0.9	-1.2 ± 1.6	-1.1 ± 1.3	-1.4 ± 1.8	-1.4 ± 1.5
10	-2.8 ± 1.7	-2.9 ± 0.8	-2.2 ± 1.7	-2.2 ± 1.0	-0.5 ± 1.6	-0.5 ± 1.3	-1.9 ± 1.9	-1.8 ± 1.7
11	-2.9 ± 2.3	-3.1 ± 0.8	-2.8 ± 2.1	-2.9 ± 1.2	-1.9 ± 1.8	-1.9 ± 1.5	-1.3 ± 2.1	-1.3 ± 1.7

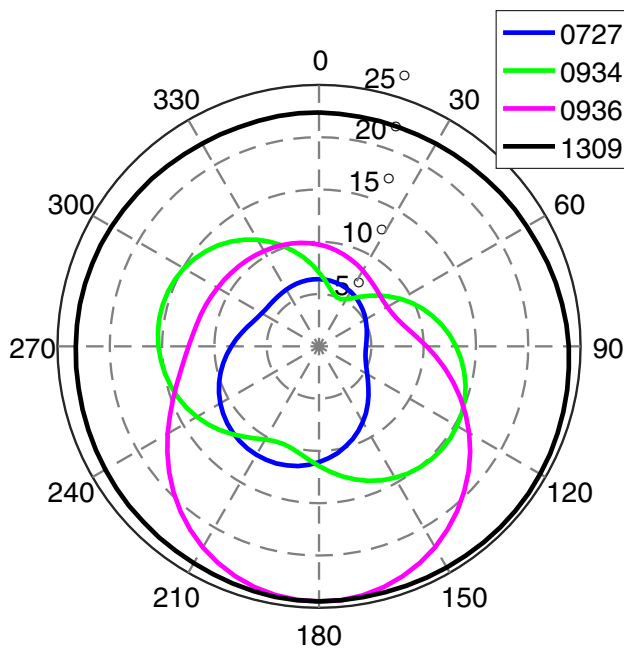


Fig. 8 Direction-dependent reference ATOS Grasselli parameter G_{ATOS} for the four rock samples

Table 4 The common area size, and the median and robust STD of reference ATOS Grasselli parameters (G_{ATOS}) calculated for 72 analysis directions

Sample	Common area (mm)	Median \pm robust STD G_{ATOS} ($^\circ$)
0727	203.3 \times 142.6	7.6 \pm 2.5
0934	244.2 \times 148.4	11.8 \pm 3.2
0936	216.7 \times 147.5	14.3 \pm 5.7
1309	213.6 \times 161.1	23.4 \pm 0.8

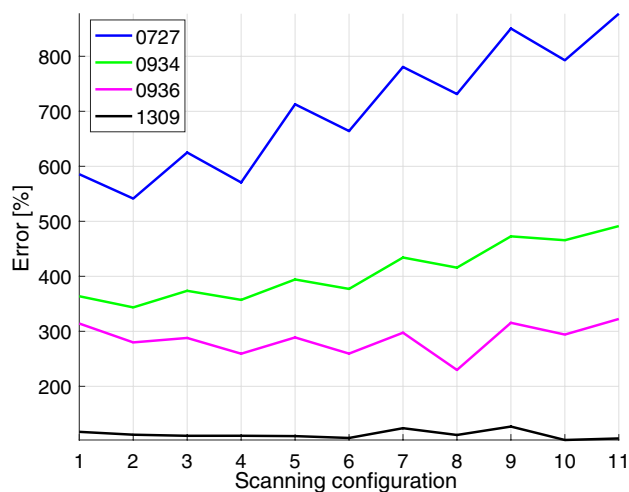


Fig. 9 Error (%) for noisy TLS surfaces of the 4 samples and 11 scanning configurations

samples. The darkest and smoothest sample 0727 is most severely influenced by the noise, while the bright and roughest sample 1309 is least influenced. The noise effect for sample 0727 increases with range, but this is not the case for sample 1309. The errors for samples 0727 and 1309 range from approximately 550–850% and 105–130%, respectively. For samples 0727, 0934, and 0936, the surface appears smoother when scanned in oblique directions (even configuration numbers).

For smoother surfaces (samples 0727 and 0934), the noise effect increases with increasing range. However, for rougher surfaces (sample 0936 and 1309), the noise effect is balanced with the smoothing effect caused by the laser beam footprint size, which increases with scanning range and incidence angle. The lower noise effect for surfaces scanned in oblique directions is a consequence of projecting the noise onto the mean plane.

4.3.3 Noise Estimation

The noise (σ_e) was estimated using Eq. (4), where first-level detail coefficients were obtained from DWT and SWT transforms of range and surface images. The dependence of σ_e on recorded intensity is for all data sets and decomposition combinations, as depicted in Fig. 10, together with the fitted curve of the one-term power-series (Wujanz et al. 2017) and the root-mean-square error (RMSE) as a measure of goodness of fit. Figure 10a, b shows these results for range and surface images, respectively.

These data show that σ_e is inversely proportional to the mean intensity, that σ_e using SWT is slightly higher than for DWT, and the σ_e values calculated from range images are less disperse and have smaller RMSE than for surface images.

These results suggest that the dependence of noise on scanning configuration and surface reflectivity can be jointly explained by the TLS measurements of intensity. Highly reflective limestone (sample 1309) and schist (sample 0936) entail higher intensity values and lower σ_e compared to dark basalt (sample 0727) and clay stone (sample 0934), which absorb laser light causing lower intensity values and, consequently, higher σ_e . However, the strong reflection of sample 0936 scanned at 10 m range in the perpendicular direction results in higher σ_e .

Figure 11 shows the σ_e dependence on the scanning configuration estimated using SWT (DWT estimates are similar and, therefore, excluded). The zig-zag pattern of σ_e calculated for surface images (Z-den) shows that oblique scans have lower σ_e than perpendicular scans. The σ_e calculated for range images (R-den) tends to increase with the range and incidence angle. Exceptions are the high σ_e for sample 0936 (configuration 8), and the low σ_e for sample 1309 (configuration 11). Possible reasons for the 0936 anomaly

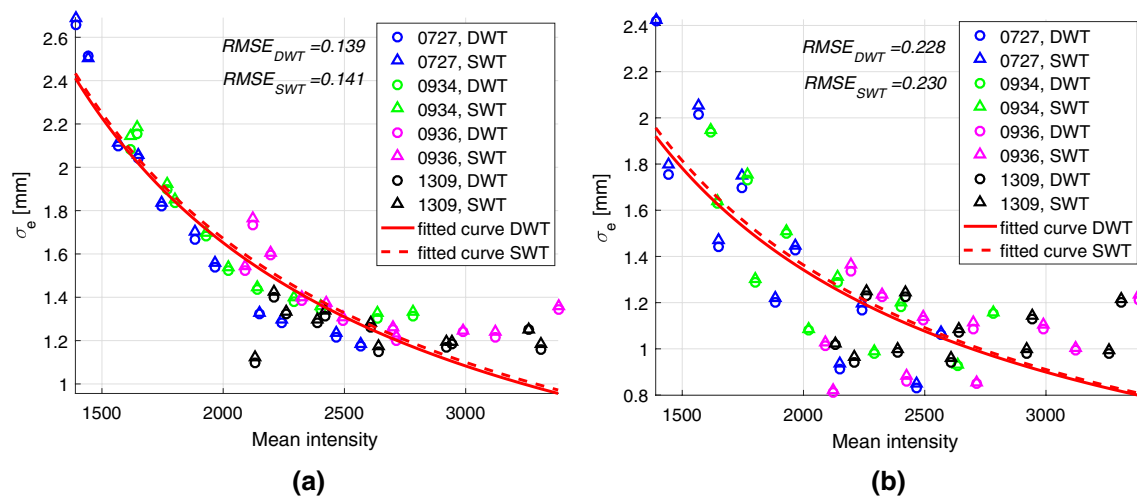


Fig. 10 Estimated noise (σ_e) for the four rock samples (color-coded) calculated from DWT (circles) and SWT (triangles) coefficients of: **a** range; and **b** surface images versus mean intensity. A one-term

power-series curve is fitted into the data and the root-mean-square error (RMSE) is shown

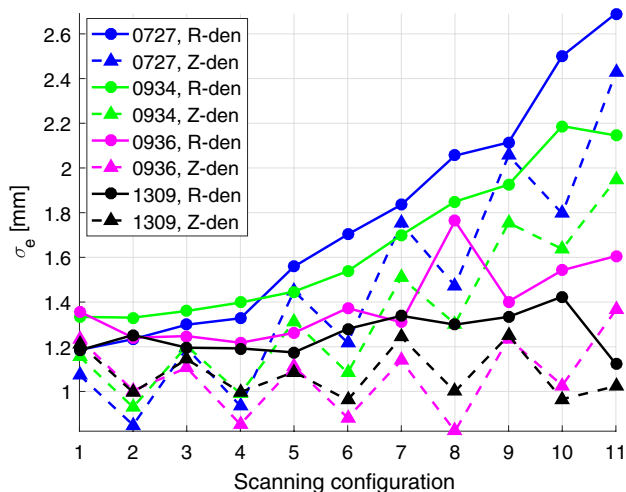


Fig. 11 Estimated noise (σ_e) for the four rock samples (color-coded) calculated from SWT coefficients of range (R-den, solid line with circles) and surface (Z-den, dashed line with triangles) images versus scanning configuration

include the high incidence angle (approximately 47°), and the 1309 anomaly may be related to low original point density of 2 mm (compared to 1 mm range image pixel size).

The results of Figs. 10 and 11 suggest that noise estimated from wavelet components of range images is more reliable than for surface images.

4.3.4 Optimal Wavelet-Denoising Procedure

To evaluate how the threshold selection methods, wavelet transform methods and denoising directions influence

wavelet-denoising results; the errors for denoised surfaces are shown in Fig. 12 and discussed below.

Threshold selection method Low thresholds preserve most of the coefficients (conservative thresholding) and result in a rougher denoised surface. High thresholds, on the opposite, remove more coefficients, thus return a smoother surface. The error depends on the actual surface roughness and scanning configuration. With the Grasselli parameter overestimated up to 350%, the penalised low threshold is inefficient in case of sample 0727. This threshold is better suited for rougher sample 1309, where the error varies approximately between 70% and -50%. The local fixed form and global penalised high thresholds return similar errors, which are the smallest for all the scanning configurations in case of smoother samples 0727 and 0934. However, those thresholds underestimate the actual surface roughness of rougher samples 0936 and 1309, especially for longer ranges.

Possible reasons for underestimated Grasselli parameters for rougher samples include the removal of some surface details due to high thresholds, and increase in the laser beam footprint size with scanning range. A solution for the first cause is to apply more conservative thresholds like penalised medium or penalised low (Bitenc et al. 2015b).

DWT versus SWT Denoised surfaces using the SWT are smoother than for the DWT. The reason is that the SWT reconstruction process averages slightly shifted DWTs. Because the SWT error is mostly smaller compared to the DWT for short ranges and their error differences are relatively small for longer ranges, the SWT is a preferred

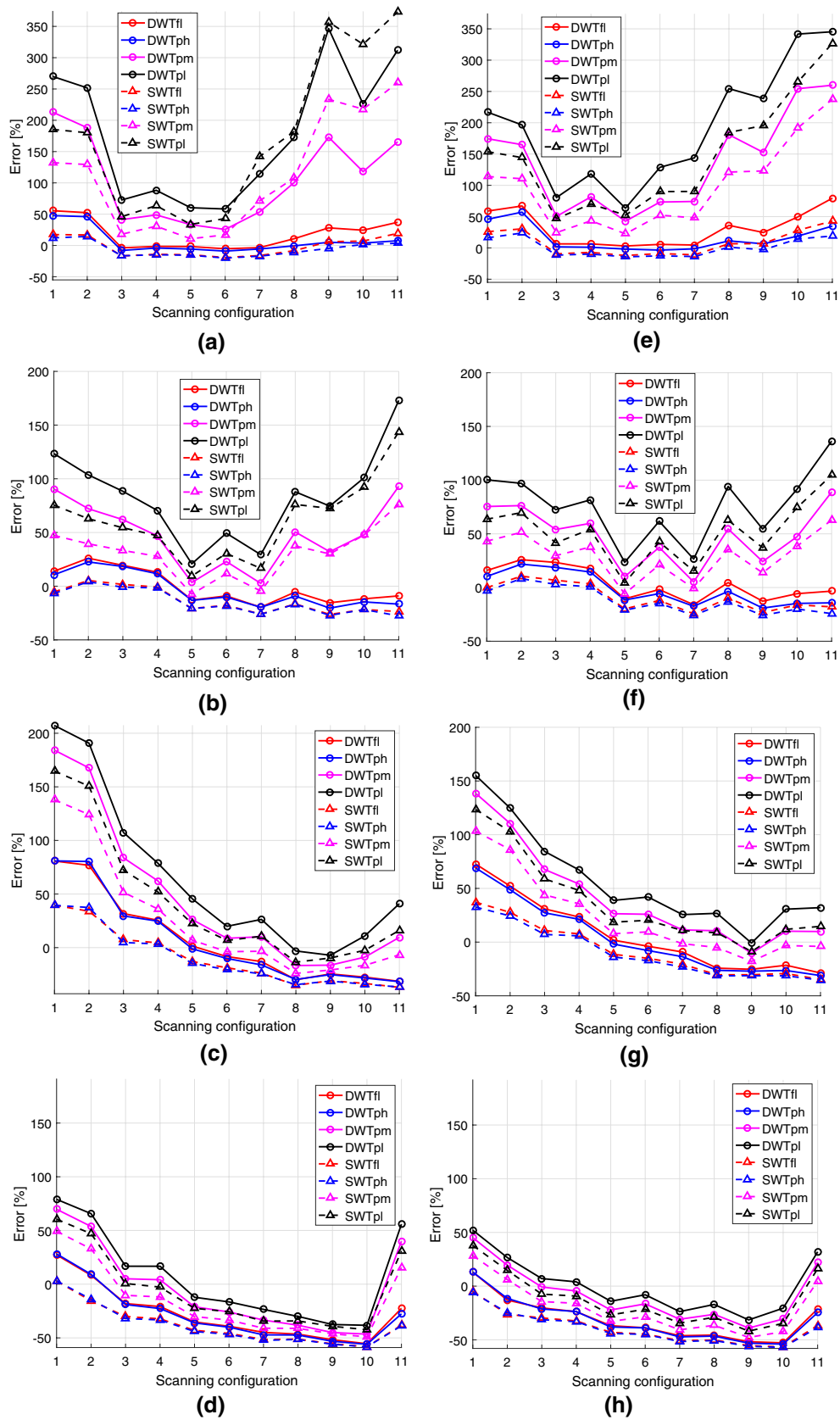


Fig. 12 Error (%) of range (a–d) and surface (e–h) denoised surfaces using DWT (solid line with circles) and SWT (dashed line with triangles) in combination with the four thresholds (color-coded lines), local fixed form (fl), and global penalised high (ph), medium (pm) and low (pl), versus scanning configuration for sample a, e 0727, b, f 0934, c, g 0936, and d, h 1309

wavelet transform for its advantages as stationary invariance and reduced edge effect.

Range versus surface denoising The errors for range and surface denoising results are shown in Fig. 13. The results show a considerable amount of noise removal when compared to the error of noisy TLS surfaces shown in Fig. 9. The Grasselli parameter of denoised surfaces for samples 0727, 0934, and 0936 is over- or underestimated by maximum 39%, and for the roughest sample 1309, the parameter is underestimated up to 57%. For most samples and scanning configurations, range-denoised surfaces appear smoother than surface denoised, as a consequence of larger σ_e and, thus, higher thresholds.

5 Summary and Conclusions

In this paper, advanced wavelet-denoising methods were applied to remove TLS range noise, to capture surface morphology details for quantifying rock surface roughness. The TLS data were acquired at different ranges and incidence angles, for four rock samples having different roughness and reflectivity. Two wavelet transforms, DWT and SWT, were used in combination with four threshold selection methods. Denoising was executed in the direction of range measurements (range denoising) and in direction of surface roughness measurements perpendicular to the mean plane (surface denoising). By systematically comparing reference ATOS surfaces to noisy and denoised TLS surfaces, the influence of noise and noise estimations from the TLS data has been quantified, and the success of wavelet-denoising procedures has been demonstrated.

The analyses have shown roughness over-estimation due to the TLS noise, especially for smoother natural rock surfaces. By applying wavelet-denoising procedures, TLS data were substantially improved and more reliable estimates of rock surface roughness were obtained. However, the success depends on the threshold value defined by the threshold selection method and noise estimation.

The results of this study suggest that the optimal threshold selection method should be chosen based on surface roughness properties. High thresholds, including fixed-form

or penalised high, successfully eliminated the high noise effect for smoother surfaces. More conservative thresholds (removing less coefficients), including penalised low, have shown to be more appropriate for rougher surfaces, where the noise is mixed with surface details.

The TLS range noise is not precisely known a priori and depends on surface reflectivity and scanning geometry. In this research, the noise (σ_e) was estimated with the Median Absolute Deviation of the first-level detail coefficients obtained from the DWT and SWT of range and surface images. The results show that σ_e values calculated from both wavelet transforms are similar and are, especially when using range images, highly correlated with the raw intensity values. The observed inversely proportional functional relationship coincides with the intensity-based stochastic model presented in the previous research (Wujanz et al. 2017). However, the σ_e depends on the image construction method. The grid (pixel) size should be equal to or bigger than the TLS sampling interval, and the Nearest-Neighbour (NN) interpolation method is preferred to the mean. Our initial studies showed that adopting the mean value within a radius results in lower σ_e as compared to NN.

The comparative analysis of denoised surfaces using DWT and SWT shows that the SWT surfaces are smoother. This finding is attributed to the SWT reconstruction algorithm, which involves the averaging of slightly shifted DWTs. Since the differences of surface roughness are small, the SWT is preferred due to its stationary invariance and ability to reduce edge effects.

Finally, the main finding of this research is that range denoising outperforms surface denoising, because it returns more reliable σ_e for arbitrary scanning configurations. If the TLS polar coordinates are available, denoising should preferably be performed in the range direction.

The Grasselli parameter is highly sensitive to TLS noise. Fractal representations of surface features have also been found to be sensitive to noise (Khoshelham et al. 2011), as well as roughness values obtained through virtual compass and disc-clinometer measurements (Bitenc et al. 2015c). Further research is warranted to assess the relative sensitivity of alternate roughness parameters to TLS noise.

To establish the optimal scanning configuration for discerning the rock surface details, the combined influence of TLS noise and the laser beam footprint size are deserving of future research. This is because the influence of noise is attenuated by the smoothing effect of the footprint size, particularly for rough surfaces combined with increasing scanning range and incidence angle. Constructing a full 2.5D image from a scattered 3D point cloud remains a challenge in applying image denoising methods to TLS data. A possible solution is to utilize diffusion wavelets (Coifman and Maggioni 2006), which are an extension of the classical

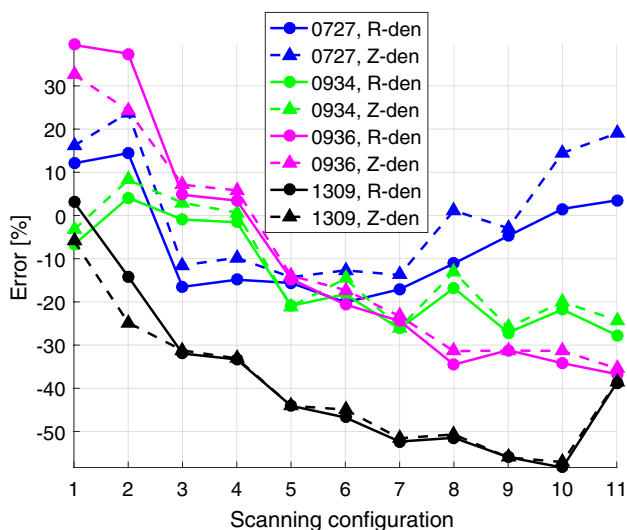


Fig. 13 Error (%) of range (solid line with circles) and surface (dashed line with triangles)-denoised TLS data using SWT with global penalised high threshold versus scanning configuration for the four samples (color-coded)

wavelet transform and have been shown to function well for discrete structures such as point.

Acknowledgements Open access funding provided by Graz University of Technology. The authors would like to acknowledge the Slovenian National Building Institute and Civil Engineering Institute that enabled data acquisition with ATOS measuring system.

Open Access This article is distributed under the terms of the Creative Commons Attribution 4.0 International License (<http://creativecommons.org/licenses/by/4.0/>), which permits unrestricted use, distribution, and reproduction in any medium, provided you give appropriate credit to the original author(s) and the source, provide a link to the Creative Commons license, and indicate if changes were made.

References

- Baker BR, Gessner K, Holden E-J, Squelch AP (2008) Automatic detection of anisotropic features on rock surfaces. *Geosphere* 4:418–428
- Bandis SC, Lumsden AC, Barton NR (1983) Fundamentals of rock joint deformation. *Int J Rock Mech Min Sci Geomech Abstr* 20:249–268. [https://doi.org/10.1016/0148-9062\(83\)90595-8](https://doi.org/10.1016/0148-9062(83)90595-8)
- Barton N, Choubey V (1977) The shear strength of rock joints in theory and practice. *Rock Mech Rock Eng* 10:1–54. <https://doi.org/10.1007/bf01261801>
- Belem T, Homand-Etienne F, Souley M (2000) Quantitative Parameters for Rock Joint Surface Roughness. *Rock Mech Rock Eng* 33:217–242. <https://doi.org/10.1007/s006030070001>
- Birgé L, Massart P (1997) From model selection to adaptive estimation. In: Pollard D, Torgersen E, Yang GL (eds) *Festschrift for Lucien Le Cam*. Springer, New York, pp 55–87
- Bitenc M, Kieffer DS, Khoshelham K (2015a) Evaluation of wavelet denoising methods for small-scale joint roughness estimation using terrestrial laser scanning. II-3/W5:81–88. <https://doi.org/10.5194/isprsannals-II-3-W5-81-2015>
- Bitenc M, Kieffer DS, Khoshelham K (2015b) Estimating joint roughness using wavelet-based denoised terrestrial laser scanning data. In: *Future development of rock mechanics*. Austrian Society for Geomechanics, pp 517–522
- Bitenc M, Kieffer DS, Khoshelham K, Vežočanik R (2015c) Quantification of rock joint roughness using terrestrial laser scanning. In: Lollino G, Giordan D, Thuro K et al (eds) *Engineering geology for society and territory*, vol 6. Applied Geology for Major Engineering Projects. Springer International Publishing, Cham, pp 835–838
- Bitenc M, Kieffer DS, Khoshelham K (2016) Evaluation of wavelet and non-local mean denoising of terrestrial laser scanning data for small-scale joint roughness estimation. *Int Arch Photogramm Remote Sens Spat Inf Sci XLI- B3:181–186*. <https://doi.org/10.5194/isprs-archives-XLI-B3-181-2016>
- Buades A, Coll B, Morel JM (2004) On image denoising methods. Technical Note, CMLA (Centre de Mathématiques et de Leurs Applications)
- Buades A, Coll B, Morel J (2005) A review of image denoising algorithms, with a new one. *Multiscale Model Simul* 4:490–530. <https://doi.org/10.1137/040616024>
- Candela T, Renard F, Bouchon M et al (2009) Characterization of fault roughness at various scales: implications of three-dimensional high resolution topography measurements. *Pure Appl Geophys* 166:1817–1851. <https://doi.org/10.1007/s00024-009-0521-2>
- Carrivick J, Smith M, Quincey D (2016) *Structure from motion in the geosciences*. Wiley-Blackwell, Chichester
- CloudCompare (2018) CloudCompare—subsample tool. <http://www.cloudcompare.org/doc/wiki/index.php?title=Edit%5CSubsample>. Accessed 11 June 2018
- Coifman RR, Donoho DL (1995) *Translation-invariant de-noising*. Springer, New York
- Coifman RR, Maggioni M (2006) Diffusion wavelets. *Appl Comput Harmon Anal* 21:53–94. <https://doi.org/10.1016/j.acha.2006.04.004>
- Daubechies I (1992) *Ten lectures on wavelets*. Society for Industrial and Applied Mathematics, Philadelphia
- Donoho DL (1995) De-noising by soft-thresholding. *Inf Theory IEEE Trans Inf Theory* 41:613–627. <https://doi.org/10.1109/18.382009>
- Donoho DL, Johnstone IM (1995) Adapting to unknown smoothness via wavelet shrinkage. *J Am Stat Assoc* 90:1200–1224
- Fardin N, Stephansson O, Feng Q (2004) Application of a new in situ 3D laser scanner to study the scale effect on the rock joint surface roughness. *Int J Rock Mech Min Sci* 41:329–335
- Fecker E, Rengers N (1971) Measurement of large scale roughness of rock planes by means of profilograph and geological compass. In: *Proceedings symposium on rock fracture*, pp 1–18
- Grasselli G (2001) *Shear strength of rock joints based on quantified surface description*, Ph.D. thesis. EPF Lausanne, Lausanne
- Grasselli G, Wirth J, Egger P (2002) Quantitative three-dimensional description of a rough surface and parameter evolution with shearing. *Int J Rock Mech Min Sci* 39:789–800. [https://doi.org/10.1016/s1365-1609\(02\)00070-9](https://doi.org/10.1016/s1365-1609(02)00070-9)
- Gyaourova A, Kamath C, Fodor IK (2002) Undecimated wavelet transforms for image de-noising. Rep Lawrence Livermore Natl Lab, Livermore, p 18
- Haneberg WC (2007) Directional roughness profiles from three-dimensional photogrammetric or laser scanner point clouds. In: Eberhardt E (ed) *1st Canada-U.S rock mechanics symposium*, pp 1001–1006

- Hartley R, Zisserman A (2003) Multiple view geometry in computer vision, 2nd edn. Cambridge University Press, New York
- Hong E-S, Lee I-M, Lee J-S (2006) Measurement of rock joint roughness by 3D scanner. *Geotech Test J* 29:482–489
- Huang SL, Oelfke SM, Speck RC (1992) Applicability of fractal characterization and modelling to rock joint profiles. *Int J Rock Mech Min Sci Geomech Abstr* 29:89–98. [https://doi.org/10.1016/0148-9062\(92\)92120-2](https://doi.org/10.1016/0148-9062(92)92120-2)
- ISRM (1978) Suggested methods for the quantitative description of discontinuities in rock masses. *Int J Rock Mech Min Sci Geomech Abstr* 15:319–368
- Khoshelham K, Altundag D, Ngan-Tillard D, Menenti M (2011) Influence of range measurement noise on roughness characterization of rock surfaces using terrestrial laser scanning. *Int J Rock Mech Min Sci* 48:1215–1223. <https://doi.org/10.1016/j.ijrmms.2011.09.007>
- Krahn J, Morgenstern NR (1979) The ultimate frictional resistance of rock discontinuities. *Int J Rock Mech Min Sci Geomech Abstr* 16:127–133. [https://doi.org/10.1016/0148-9062\(79\)91449-9](https://doi.org/10.1016/0148-9062(79)91449-9)
- Kregar K, Grigillo D, Kogoj D (2013) High precision target center determination from a point cloud. In: *ISPRS annals of the photogrammetry, remote sensing and spatial information sciences*, pp 139–144
- Kulatilake P, Balasingam P, Park J, Morgan R (2006) Natural rock joint roughness quantification through fractal techniques. *Geotech Geol Eng* 24:1181–1202. <https://doi.org/10.1007/s10706-005-1219-6>
- Lee H-S, Ahn K-W (2004) A prototype of digital photogrammetric algorithm for estimating roughness of rock surface. *Geosci J* 8:333–341. <https://doi.org/10.1007/bf02910253>
- Lee YH, Carr JR, Barr DJ, Haas CJ (1990) The fractal dimension as a measure of the roughness of rock discontinuity profiles. *Int J Rock Mech Min Sci Geomech Abstr* 27:453–464. [https://doi.org/10.1016/0148-9062\(90\)90998-h](https://doi.org/10.1016/0148-9062(90)90998-h)
- Lichti DD, Jamtsho S (2006) Angular resolution of terrestrial laser scanners. *Photogramm Rec* 21:141–160. <https://doi.org/10.1111/j.1477-9730.2006.00367.x>
- Maerz NH, Franklin JA, Bennett CP (1990) Joint roughness measurement using shadow profilometry. *Int J Rock Mech Min Sci Geomech Abstr* 27:329–343. [https://doi.org/10.1016/0148-9062\(90\)92708-m](https://doi.org/10.1016/0148-9062(90)92708-m)
- Mills G, Fotopoulos G (2013) On the estimation of geological surface roughness from terrestrial laser scanner point clouds. *Geosphere* 9:1410–1416. <https://doi.org/10.1130/GES00918.1>
- Milne D, Hawkes C, Hamilton C (2009) A new tool for the field characterization of joint surfaces. In: *Proceedings of the 3rd CANUS rock mechanics symposium*, Toronto
- Myers NO (1962) Characterization of surface roughness. *Wear* 5:182–189. [https://doi.org/10.1016/0043-1648\(62\)90002-9](https://doi.org/10.1016/0043-1648(62)90002-9)
- Patton FD (1966) Multiple modes of shear failure in rock. *International Society for Rock Mechanics*, pp 509–513
- Pfeifer N, Briese C (2007) Geometrical aspects of airborne laser scanning and terrestrial laser scanning. *Int Arch Photogramm Remote Sens Spat Inf Sci* 36:311–319
- Pollyea RM, Fairley JP (2011) Estimating surface roughness of terrestrial laser scan data using orthogonal distance regression. *Geology* 39:623–626. <https://doi.org/10.1130/G32078.1>
- Poropat G (2009) Measurement of surface roughness of rock discontinuities. In: *Proceedings of the 3rd CANUS rock mechanics symposium*, Toronto
- Power WL, Tullis TE (1991) Euclidean and fractal models for the description of rock surface roughness. *J Geophys Res* 96:415–424. <https://doi.org/10.1029/90jb02107>
- Priest SD (1993) Discontinuities and rock deformability. In: *Discontinuity analysis for rock engineering*. Springer Netherlands, pp 300–339
- Rahman Z, Slob S, Hack R (2006) Deriving roughness characteristics of rock mass discontinuities from terrestrial laser scan data
- Reeves MJ (1985) Rock surface roughness and frictional strength. *Int J Rock Mech Min Sci Geomech Abstr* 22:429–442. [https://doi.org/10.1016/0148-9062\(85\)90007-5](https://doi.org/10.1016/0148-9062(85)90007-5)
- Renard F, Voisin C, Marsan D, Schmittbuhl J (2006) High resolution 3D laser scanner measurements of a strike-slip fault quantify its morphological anisotropy at all scales. *Geophys Res Lett* 33:L04305. <https://doi.org/10.1029/2005gl025038>
- Schulz T, Ingensand H, Wunderlich T (2008) Calibration of a terrestrial laser scanner for engineering geodesy. *Institut für Geodäsie und Photogrammetrie an der Eidgenössischen Technischen Hochschule, Zürich*
- Seidel JP, Haberfield CM (1995) Towards an understanding of joint roughness. *Rock Mech Rock Eng* 28:69–92. <https://doi.org/10.1007/bf01020062>
- Smigiel E, Alby E, Grussenmeyer P (2011) TLS data denoising by range image processing. *Photogramm Rec* 26:171–189. <https://doi.org/10.1111/j.1477-9730.2011.00631.x>
- Soudarissanane S, Lindenbergh R, Menenti M, Teunissen P (2011) Scanning geometry: Influencing factor on the quality of terrestrial laser scanning points. *ISPRS J Photogramm Remote Sens* 66:389–399. <https://doi.org/10.1016/j.isprsjprs.2011.01.005>
- Starck J-L, Elad M, Donoho DL (2004) Redundant multiscale transforms and their application for morphological component separation. In: *Advances in imaging and electron physics*, 1st edn. p 400
- Tatone BSA, Grasselli G (2009) A method to evaluate the three-dimensional roughness of fracture surfaces in brittle geomaterials. *Rev Sci Instrum* 80:125110–125110
- Tesfamariam EK (2007) Comparing discontinuity surface roughness derived from 3D terrestrial laser scan data with traditional field-based methods. *International Institute for Geo-information Science and Earth Observation, Enschede*
- Tse R, Cruden DM (1979) Estimating joint roughness coefficients. *Int J Rock Mech Min Sci Geomech Abstr* 16:303–307. [https://doi.org/10.1016/0148-9062\(79\)90241-9](https://doi.org/10.1016/0148-9062(79)90241-9)
- Wagner W (2005) Physical principles of airborne laser scanning. In: Kraus K (ed) *University course: laser scanning—data acquisition and modeling*. Institute of Photogrammetry and Remote Sensing
- Wu TH, Ali EM (1978) Statistical representation of joint roughness. *Int J Rock Mech Min Sci Geomech Abstr* 15:259–262. [https://doi.org/10.1016/0148-9062\(78\)90958-0](https://doi.org/10.1016/0148-9062(78)90958-0)
- Wujanz D, Burger M, Mettenleiter M, Neitzel F (2017) An intensity-based stochastic model for terrestrial laser scanners. *ISPRS J Photogramm Remote Sens* 125:146–155. <https://doi.org/10.1016/j.isprsjprs.2016.12.006>
- Zhang Y, Liu J, Li M, Guo Z (2014) Joint image denoising using adaptive principal component analysis and self-similarity. *Inf Sci* 259:128–141. <https://doi.org/10.1016/j.ins.2013.08.002>

Publisher's Note Springer Nature remains neutral with regard to jurisdictional claims in published maps and institutional affiliations.